Acta Oceanol. Sin., 2019, Vol. 38, No. 6, P. 124–131
https://doi.org/10.1007/s13131-019-1387-5
http://www.hyxb.org.cn
E-mail: hyxbe@263.net

Experimental investigation on the optical remote sensing images of internal solitary waves with a smooth surface

Yuan Mei[1], Jing Wang[1]*, Songsong Huang[1], Haidi Mu[2], Xu Chen[2]

[1] College of Information Science and Engineering, Ocean University of China, Qingdao 266100, China

[2] College of Oceanic and Atmospheric Sciences, Ocean University of China, Qingdao 266100, China

Received 1 March 2018; accepted 2 April 2018

Abstract

The parameter inversion of internal solitary waves (ISWs) based on optical remote sensing images is a key work. A new approach is proposed and demonstrated for simulating the optical remote sensing images of ISWs with a smooth surface in the laboratory. An optical remote sensing simulation system used to detect ISWs is constructed by a two-dimensional ISW flume, a LED (light emitting diode) light source and two CCD (charge coupled device) cameras. The optical remote sensing images of the horizontal surface and ISWs propagation images of a vertical side are detected simultaneously, which aims to explore the response of optical remote sensing corresponding to ISWs with the smooth surface. The results show that during the propagation of ISWs, dark pattern images are obtained by CCD 1 camera. The characteristics of the dark patterns vary along with the incident angle of the light source. The characteristic parameters of the optical remote sensing images correspond to the wave factors of vertical profiles. The experiment also shows a positive correlation between the dark pattern width and the half wave width under different amplitudes of ISWs. The system has the advantages of clear phenomenon and high repeatability, which provides the scientific basis for quantitative investigation on imaging mechanism of ISW by optical remote sensing.

Key words: internal solitary wave, optical remote sensing image, dark pattern, half wave width, wave factors

Citation: Mei Yuan, Wang Jing, Huang Songsong, Mu Haidi, Chen Xu. 2019. Experimental investigation on the optical remote sensing images of internal solitary waves with a smooth surface. Acta Oceanologica Sinica, 38(6): 124–131, doi: 10.1007/s13131-019-1387-5

1 Introduction

The internal solitary wave (ISW), occurring in the density stratified sea water, will lead to the roughness and the slope of the sea surface during the propagation process. Convergence zones and divergence zones of a sea surface wave will be formed under the influence of the capillary wave from the sea surface wind field. Hence the ISW will display as light-dark patterns on optical remote sensing images. In recent years, China has launched a series of optical remote sensing satellites such as GF-1, GF-2 and GF-4, providing abundant observational data with high spatio-temporal resolution and multi-spectral source to develop new approaches for the detection of ISWs. Currently, the optical remote sensing images are mainly used to detect and estimate the spatial and temporal distributions of ISWs (Cho et al., 2016; Cai et al., 2014). In contrast, the parameters inversion of ISWs based on optical remote sensing are relatively rare. Nevertheless, the parameters extraction from the optical remote sensing images, including the amplitude, half wave width, and propagation velocity of ISWs, are of great significance in oceanography. In this work, a series of experiments were performed in a two-dimensional flume to investigate on the optical remote sensing images of ISWs with the smooth surface, which provide an elementary reference on imaging mechanism of ISW by optical remote sensing.

At an early stage, Cox and Munk (1954) collected the aerial photographs of sun glitter, quantitatively measured a sea surface roughness. The obtained statistics of a radiance and slope probability distribution laid a theoretical foundation for the optical remote sensing imaging mechanism. On the basis of the Cox-Munk model, Melsheimer and Keong (2001) studied the change of a sea surface convergence and divergence under different zenith angles and sensor receiving angles, further discussed the optical remote sensing imaging mechanism of ISW. Jackson and Alpers (2010) introduced the concept of the sensor critical angle in optical remote sensing. When the geometric imaging changes through the critical angle, surface features experience brightness inversion. According to a large number of optical remote sensing images (Alford et al., 2015; Cai et al., 2011; Yang et al., 2017; Wang et al., 2013) and field experiment results (Alford et al., 2010; Huang et al., 2014), combined with numerical simulation modeling (Bourgault et al., 2016; Hsieh et al., 2016), wave parameters such as the amplitude of ISWs in the South China Sea had been calculated (Song et al., 2010; Wang et al., 2012), but deviations still exist. Because optical remote sensing is affected by clouds, sea conditions, relative position between the sun and the sensor, it is difficult to match images and field experiments, which brings numerous obstacles to research work. Therefore, a new approach was brought out to simulate the optical remote sensing images of ISWs with the smooth surface in the laboratory.

In recent years, research methods on the generation and propagation of ISWs in the laboratory have also been mature. The main focus for scholars is on exploring the generation mech-

Foundation item: The National Key Research and Development Program of China under contract No. 2017YFC1405600; the National Natural Science Foundation of China under contract No. 41476001.
*Corresponding author, E-mail: wjing@ouc.edu.cn

anism, propagation and dissipation of ISWs by using the particle image velocity (PIV) method (Dossmann et al., 2016). Chen (2012) surveyed the terrain, the incident angle and sensitive parameters of ISWs, with the combination of field data and kinematics theory. To further understand the generation, propagation and dissipation of ISWs, a real marine environment was simulated in a flume system. Kodaira et al. (2016) studied applicability of different models for ISWs in a two-layer free surface fluid system with silicone oil and water. The strong nonlinear MCC-FS model was better than the weakly nonlinear KdV model to describe the large amplitude ISW. The resonance mechanism between a short surface wave and the ISW propagated at the two-layer fluid interface was also presented. These experiments explored the generation and propagation of ISWs in the flume, which laid a good foundation for our work. Therefore, experimental investigation on the optical remote sensing images of ISWs with a smooth surface is conducted. The dark pattern images in the horizontal view and wave factors in the vertical view are simultaneously measured. The characteristics of the optical remote sensing images of ISWs were investigated.

The optical remote sensing images are influenced by the cloud, the sea condition and the relative position of the sensor and the sun. The experimental investigation on the detection of ISWs by optical remote sensing in the laboratory aims at exploring the relationship between the optical remote sensing parameters and ISW factors. The main contents of this paper are organized as follows: Section 2 presented the details of an experiment system. A LED (light emitting diode) surface light source was used to simulate the parallel beams of the sun. A gravity collapse method was used to generate ISWs in a two-layer water. Two CCD (charge coupled device) cameras were designed to record the horizontal and vertical information during the propagation of ISWs. Section 3 presented collected image data. The relationship between the dark pattern width and the half wave width was explored. The change of the dark patterns with different incident angles was also analyzed. The conclusions were presented in Section 4.

2 Experimental setup

The process of detection of ISWs by optical remote sensing can be assigned as two steps. First, the tilt of the sea surface is induced by the propagation of ISWs in the pycnocline. Then the convergence and divergence of surface capillary waves are modulated, bright and dark stripes are recorded on the optical remote sensing images. In this work, an experimental setup is designed to investigate the mechanism of the optical remote sensing response of ISWs with the smooth surface, corresponding to the first step mentioned above, which indicates that there is no capillary wave effect resulting from the surface wind field. The experimental system is designed and shown in Fig. 1. The white LED surface light source was severally placed at the right end of the flume. The quasi-parallel beams emitted by the LED source can be seen as sunlight incident on the sea surface. Two CCD cameras are arranged on the top and side of flume center, respectively. The images of free surface changes caused by ISWs are taken by the CCD 1, equivalent to the role of the real optical remote sensing cameras. The propagation process of ISWs was captured by the CCD 2. When two fields of view are arranged overlap exactly, the relation between surface and vertical features induced by the propagation of ISWs can be found.

The size of flume in this experiment is 3 m×0.15 m×0.3 m. In a vertical two-cylinder tank, 0.998 g/cm^3 pure water and fixed density of 1.082 g/cm^3 saline water were prepared, respectively.

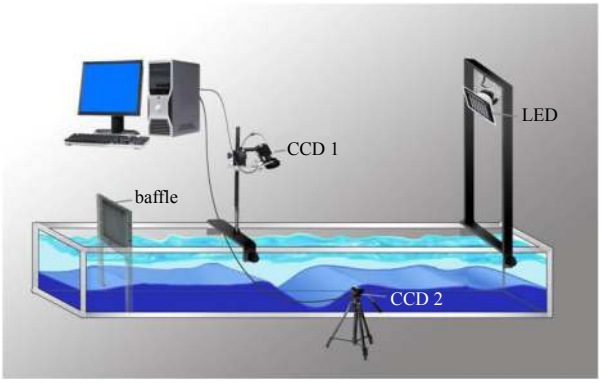

Fig. 1. The schematic diagram of simulation platform for the detection on the optical remote sensing images of ISWs with the smooth surface.

The water was put into the narrow two-dimensional flume slowly with a peristaltic pump. Stable upper and lower layers are formed to simulate a two-layer fluid ocean structure. The thickness of the upper layer is h_1=5 cm, the thickness of the lower layer is h_2= 17 cm. In the generation area of ISWs, a collapse baffle was placed at 20 cm away from the left side of the flume. The bottom of the flume was connected. The upper layer water was injected on the surface until the collapse height reached a set value. ISWs with different amplitudes are generated by different collapse heights. Meanwhile, the sponge was applied to removing the noise signal of the surface wave generated by movement of the baffle, which was placed on the right side of the baffle and the flume. When the collapse baffle was lifted rapidly and vertically, two layers water with different gravitational potential energies mixed quickly. An eddy was generated at the boundary between the upper and lower layers of water, transformed into ISWs and moved forward. Four groups of experiments with different wave collapse heights δ=8, 10, 12 and 14 cm, were performed. The raw photographs of the setup and the ISW in the two-layer water are shown in Fig. 2. The ruler was used to visually observe the vertical displacement of ISWs when they pass through the field of view.

The resolution of the CCD camera is 1 920×1 080 pixels. The field of view is 57 cm which indicates that each pixel represents 0.03 cm. The sampling frequency of these two CCD cameras is 50 Hz. The incident angles (θ_i) of light source are 60°, 45° and 30°. The receiving angle (θ_r) of the top CCD camera is 30°.

3 Results and discussion

3.1 *Dark patterns on optical remote sensing image*

CCD images were obtained as the simulated optical remote sensing images to reveal the variation of the water surface. The water in the flume, whose initial state is regarded as a smooth surface, will tilt its surface because of the ISW, which finally become the dark patterns on the simulated optical remote sensing images. A linear time series sampling method is adopted to data processing, as shown in Fig. 3, where Lines *ab* and *cd* represent the vertical and surface sampling lines of two CCD images during the propagation of the ISW, respectively.

In the case that δ=8 cm and θ_i=60°, the first 3 000 images of these two CCD cameras are recorded during the ISW propagation process. Figure 4 shows the sampling line within 1 min after a linear time series sampling operation. Figures 4a and b show the linear time series images of ISWs propagation and optical remote sensing, respectively.

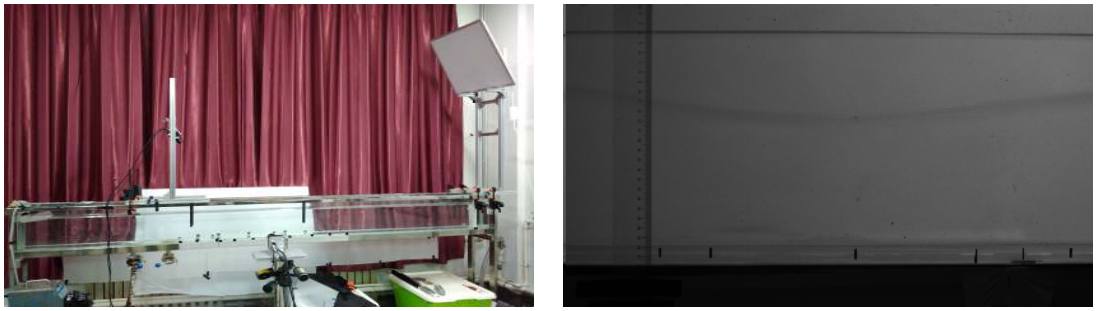

Fig. 2. The raw photograph of the experimental setup and the ISW in the two-layer water obtained by CCD 2 camera.

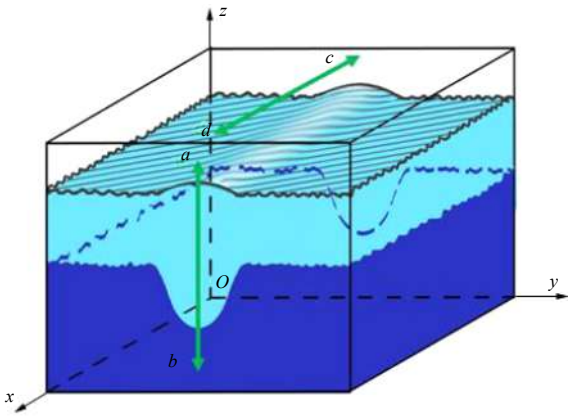

Fig. 3. The schematic diagram of linear time series sampling line.

The propagation of the ISW has been obviously observed on the images derived from both CCD cameras. It must be pointed out that the four ISWs in Fig. 4a are with two propagation directions owing to that the ISW turns back when hitting the silica wall of the flume. Namely, No. 1 and No. 3 are the ISWs propagating from left to right in the flume, and No. 2 and No. 4 are the ISWs propagating in the opposite direction. x axis represents time series (t). y axis represents the height (h) of ISWs vertical displacement recorded by the CCD 2 camera, the unit is centimeter. It can be seen from Fig. 4b, the dark patterns were obtained by the CCD 1 camera during the propagation of ISWs. y axis represents the width (w) of the dark patterns. Figure 4 also shows the coincidence between vertical displacements and patterns, which demonstrates the availability of this experimental simulation.

The dark patterns are mainly caused by the propagation of the ISW on the interface leading to a strong downward vertical displacement and accompanied with a convex surface, as illustrated in Fig. 5. The quasi-parallel beams are emitted by the LED surface light source on the top right of the flume. The angle between the ray and the vertical normal line is defined as the incident angle θ_i. The light is reflected by the free surface of the two-layer structure water and received by the CCD 1 camera. If the ISW propagates on the interface, a bulge is formed on the free surface. The direction of the specular reflected light changes, resulting in a reduction in the light power received by the CCD 1 camera and forming the dark patterns. Therefore, the dark patterns are formed on the optical remote sensing images when the

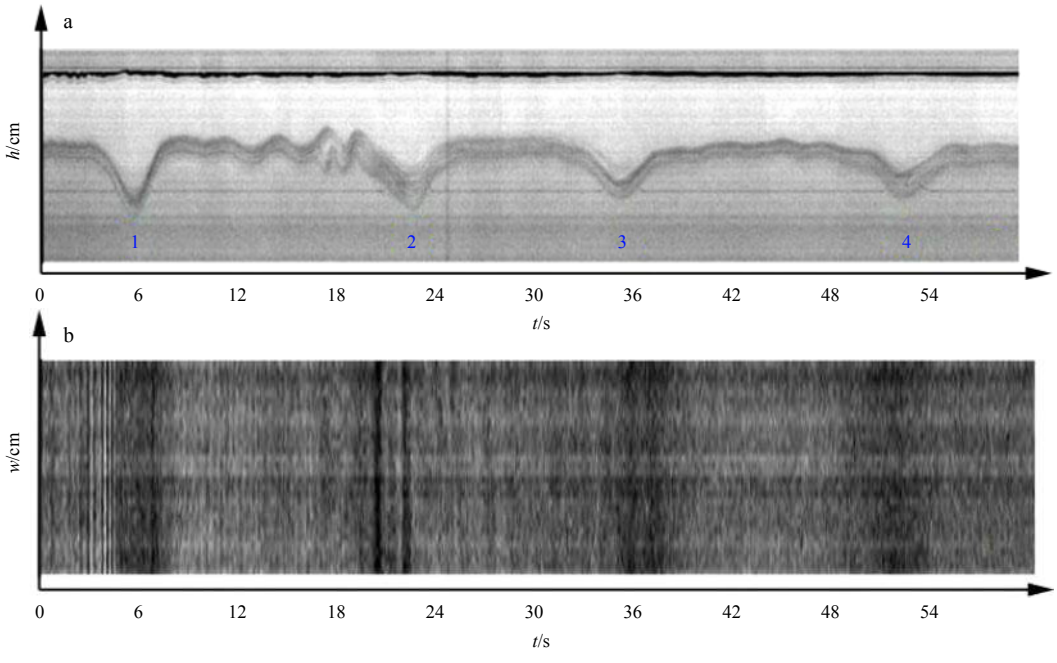

Fig. 4. The linear time series image of the ISW propagation (a) and the linear time series images of optical remote sensing (b).

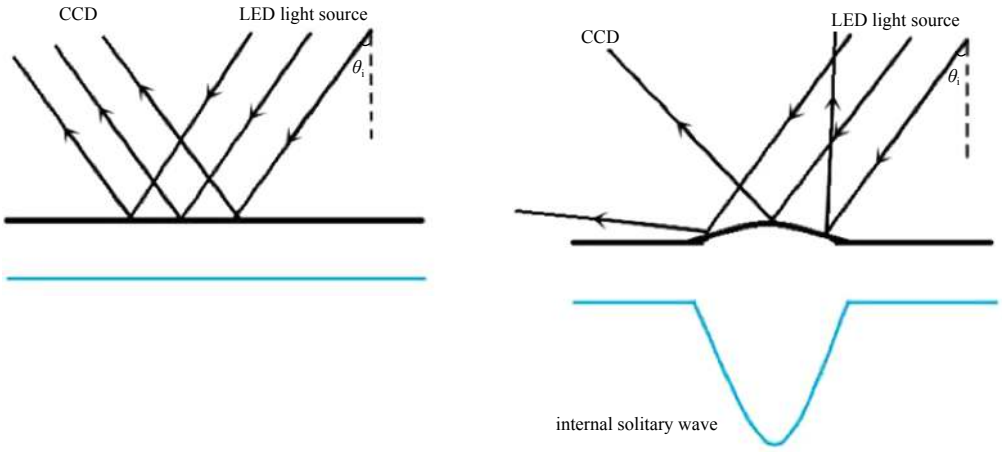

Fig. 5. The schematic diagram of the received signal intensity of the CCD.

ISW propagates through the field of view, which correspond to the vertical displacement.

3.2 *Extraction of the dark pattern characteristic parameters and ISW factors*

The experimental parameters, including the amplitude, wavelength, and half wave width of ISWs were extracted by the enlarged linear time series images taken by the CCD 2 camera, as show in Fig. 6. Lines *ef*, *fg*, *hi*, and *jk* in Fig. 6 represent the thickness of the upper layer (h_1) in the flume, the amplitude (A) of ISW, the wavelength (λ), and the wave width (two times as long as the half wave width L).

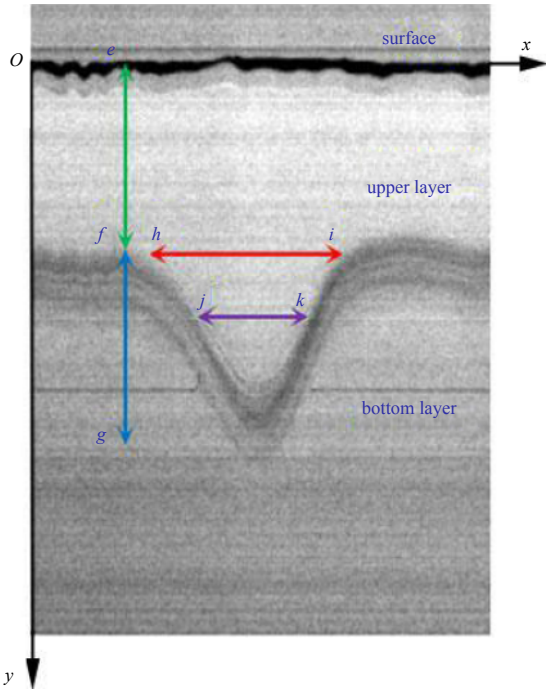

Fig. 6. Parameters extraction on the image of ISW propagation.

In this step, a gray profile curve was obtained by calculating the mean value difference between the middle part and the edge part of the patterns to minimize the background interference. The dark pattern width can be obtained. The results mentioned above and the corresponding linear time series images of the CCD 1 and the CCD 2 are shown in Fig. 7.

The dark pattern width (D) is defined as the width of the profile where the gray value decreases into half of the maximum, as Line *mn* shown in Fig. 7c. *y* axis represents the relative gray value difference of the dark patterns. Then the amplitude, the half wave width and the dark pattern width during the propagation of the ISW were calculated, as listed in Table 1. The experimental data in Table 1, shows that the amplitude decreases, the half wave width becomes larger and the corresponding dark pattern width becomes wider with the propagation of the ISW, which indicating the dramatic energy dissipation of the ISW.

3.3 *The relationship between dark pattern width and half wave width*

In order to further investigate the relationship between the dark pattern characteristic parameters and the wave factors on the simulated remote sensing images, the other four groups of experimental data with different collapse heights were extracted by the similar process with Section 3.2. The contents below mainly focus on the relationship between the dark pattern width of ISWs and the corresponding half wave width.

First of all, the synchronous linear time series of two CCD cameras are selected to calculate the calculative dark pattern width and the corresponding half wave width of them. The results, a series of scatters, are exhibited in Fig. 8 and sorted by the collapse heights.

Then the linear fitting for the scatters in Fig. 8 is carried out to get the quantitative results. It is noticed that the scattered points are relatively concentrated around the fitting line. The half wave width of ISWs and the dark pattern width are approximately positive correlated. When δ=8, 10, 12 and 14 cm, the corresponding absolute value of slope ($K_{D\text{-}L}$) are 1.83, 2.01, 1.40 and 1.13. The linear correlation coefficients are 0.64, 0.63, 0.75 and 0.70, respectively.

In order to describe the more accurate relationship among the parameters, reduce influence of the boundary layer thickness and interaction between the wave and the inner wall of the flume, the parameters of ISWs were investigated in terms of different collapse heights. So the experiment in this paper explored the relationship between the half wave width and the dark pattern width under all collapse height conditions, as shown in Fig. 9.

Figure 9 presents the connection between the half wave width

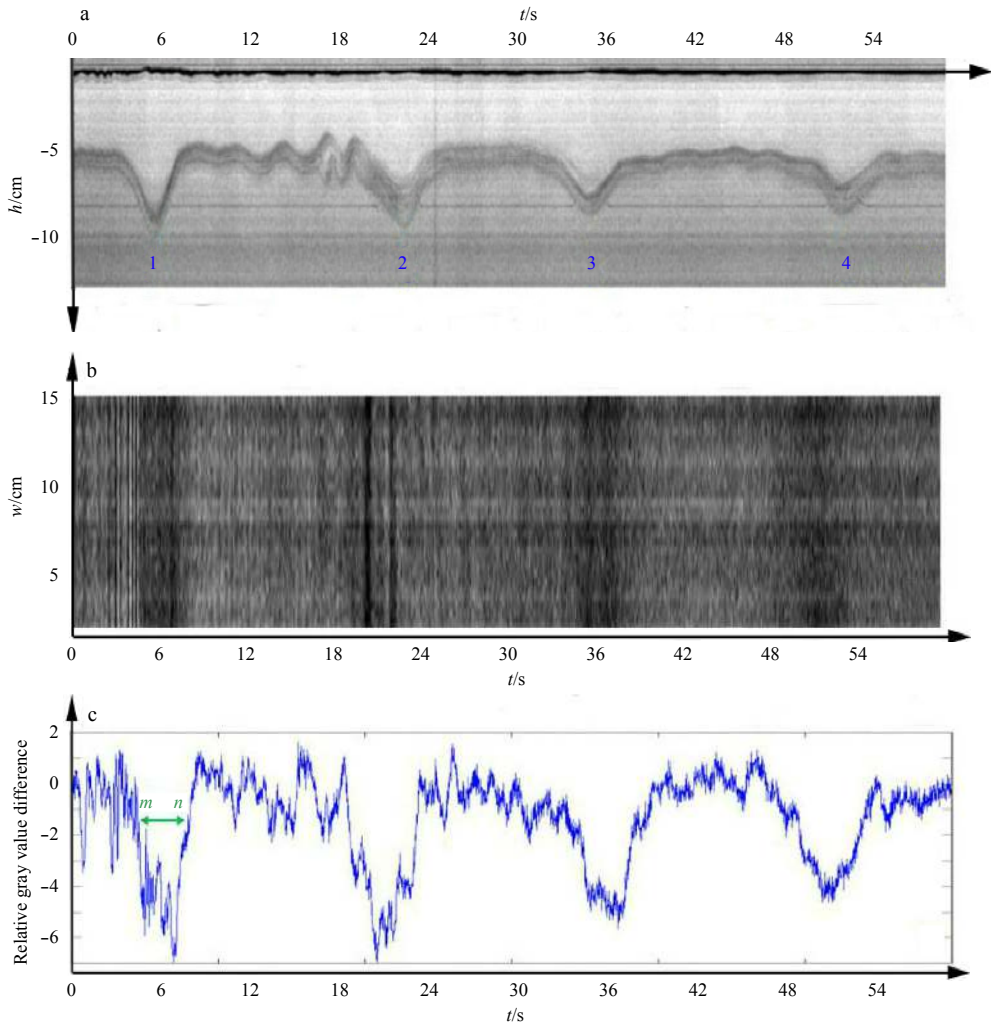

Fig. 7. Linear time series images of CCD 1 (a) and CCD 2 (b), and the relative gray level profile curve on the optical remote sensing image (c).

Table 1. Characteristic parameters of ISW

	No. 1 ISW	No. 2 ISW	No. 3 ISW	No. 4 ISW
A/mm	37.65	32.35	27.35	21.76
L/cm	22.78	27.71	29.56	29.97
D/cm	53.78	54.19	62.81	66.50

of ISWs and the dark pattern width. x axis of the fitting curve represents the half wave width L of ISWs. y axis represents the dark pattern width D. It can be seen that scattered points of the dark pattern width and the half wave width are concentrated a straight line with a positive slope, the fitting result is

$$D = 1.34L.$$

The linear correlation coefficient is 0.72. Therefore, the proportional relationship between the dark pattern width and the half wave width is positive. The equation laid a foundation for the parameters inversion of ISWs by optical remote sensing.

3.4 *Influence of incident angle of light source on dark patterns*

The structure of two-layer water and receiving angle θ_r of the CCD 1 camera remains unchanged. When the wave collapse height is δ=8 cm, the incident angle of the light source is changed to $\theta_{i,1}$=60°, $\theta_{i,2}$=45° and $\theta_{i,3}$=30°. The first 3 000 images of the CCD 1 were recorded. The sampling line corresponding to 1 min time series images is shown in Fig. 10.

Comparing the three illustrations in Fig. 10, it can be visually found that as the incident angle of the light source decreases gradually, the dark patterns become more clearly and easily distinguishable. The absolute values of gray scale based on the dark patterns of the optical remote sensing images were calculated, as listed in Table 2. With the decreasing of the incident angle, the contrast ratio of the dark patterns to background on the optical remote sensing images increases. When the absolute value of the gray difference continues to increase, the signal is more prominent. The dark patterns are most clear when $\theta_{i,3}$=30°.

4 Conclusions

In conclusion, this paper represents a new approach to simulate the optical remote sensing images of ISWs with the smooth surface in the laboratory.

In the novel experimental simulation system, ISWs are generated in a narrow two-layer fluid flume by a gravitational collapse method. Two CCD cameras, fixed on the side and top of the flume, respectively, can simultaneously observe and record the

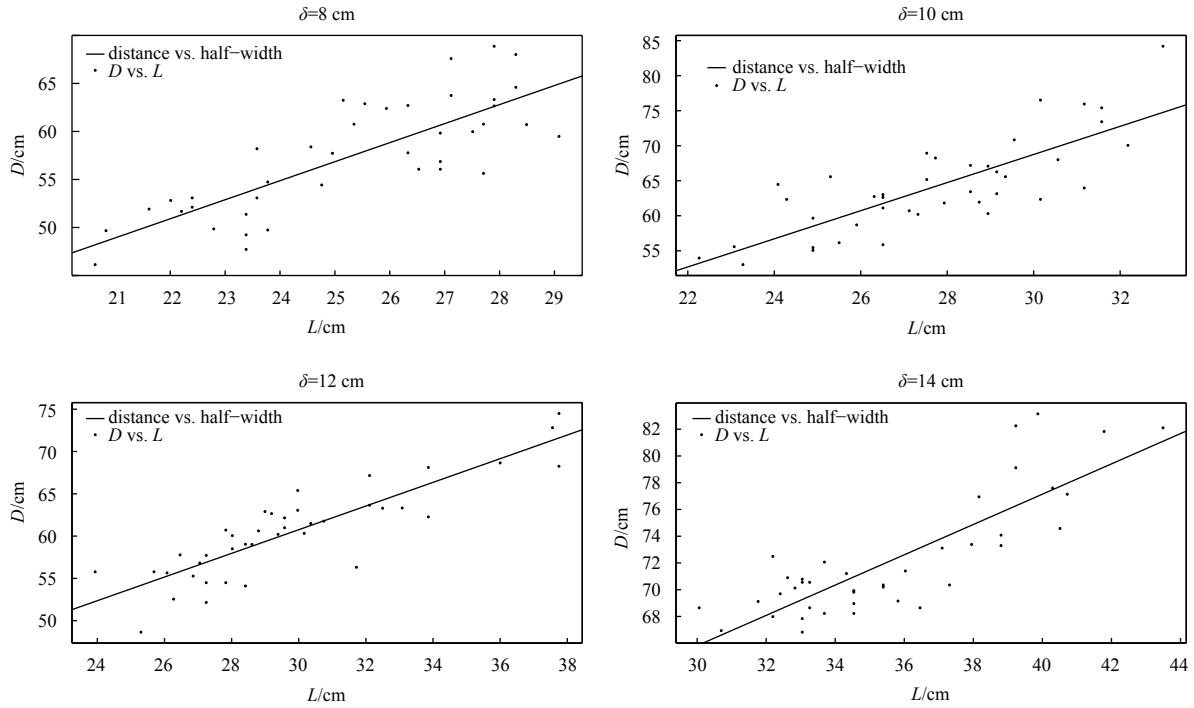

Fig. 8. The relationship between dark pattern width and half wave width of ISW.

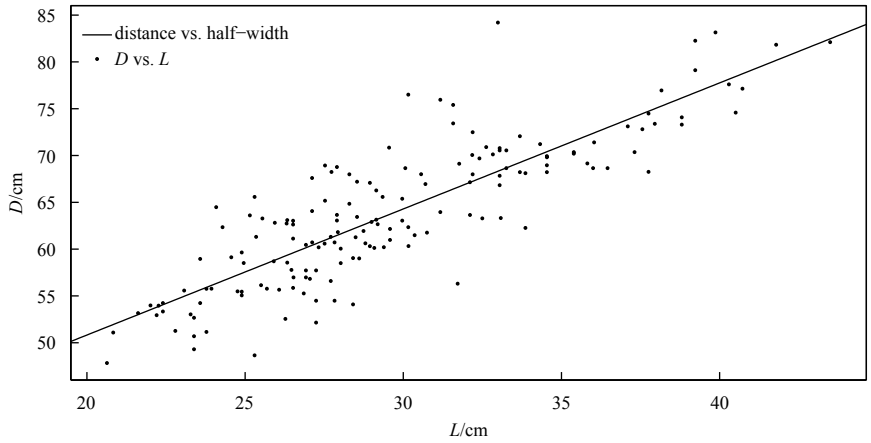

Fig. 9. The relationship between the dark pattern width and the half wave width of ISWs under different collapse heights.

vertical and horizontal signal response of ISWs. Then the recorded optical images were processed in a linear time series way. In addition, the amplitude, the half wave width, and the dark pattern width are extracted and calculated.

Experimental research in this work can be summarized as follows: (1) During the propagation of ISWs, the dark patterns are obtained by the top CCD camera. The mutual responses between the characteristics of the optical remote sensing images and images of the ISWs propagation prove the validity of the simulated detection on ISWs signal using optical remote sensing; (2) On the basis of experimental data of the smooth surface, the relationship between the dark pattern width and the half wave width is D=1.34L. The results show that the dark pattern width on the optical remote sensing images is positively correlated with the half wave width; (3) With the decreasing of incident angle of the light source, the relative gray value difference of the signal received by the CCD 1 camera is increasing, which indicates that when the contrast of the dark patterns to background increases, the amplitude inversion of ISWs is more accurate. When the incident angle of the light source is equal to the reflection angle, the dark patterns on the simulated optical remote sensing images are most clear. This work may provide a quantitative reference on parameter inversion of ISWs with the smooth surface by optical remote sensing. But the problem of the optical remote sensing simulation is not completely solved. After the wind field is added, the convergence and divergence of the surface capillary waves are generated, the more complex optical remote sensing imaging relationship between the pattern distance and the half wave width of ISWs may be obtained by experiment. Then the parameter inversion equation in the laboratory can be used in real ocean ISWs and remote sensing images based on the Reynolds criterion. The light-dark patterns are induced by ISWs in a surface wind field, which is more similar to the real ocean, will be the next step of our research.

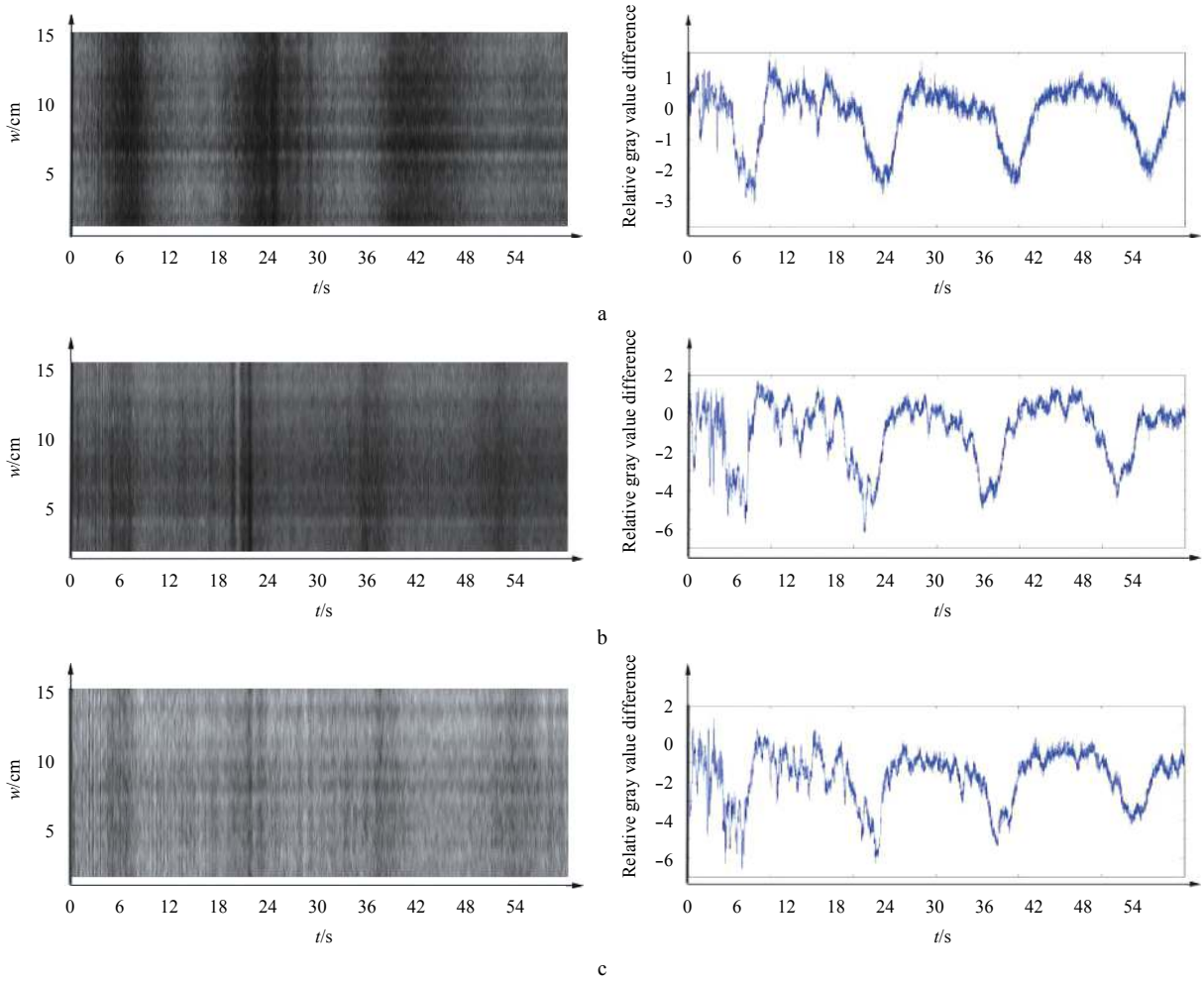

Fig. 10. Linear time series images of center line and relative gray level profile curve of the CCD 1. a. $\theta_{i,1}$=60°, b. $\theta_{i,2}$=45°, and c. $\theta_{i,3}$=30°.

Table 2. Relative gray value difference on optical remote sensing image with different incident angles of light source

	No. 1 ISW	No. 2 ISW	No. 3 ISW	No. 4 ISW	Mean value of gray difference (pixel)
$\theta_{i,1}$=60°	3.18	2.78	2.61	2.39	2.74
$\theta_{i,2}$=45°	5.79	6.26	5.04	4.77	5.46
$\theta_{i,3}$=30°	6.88	6.63	5.71	4.61	5.96

Acknowledgements

We thank the College of Oceanic and Atmospheric Sciences, Ocean University of China for providing the physical oceanography laboratory for the internal solitary wave experiments.

References

Alford M H, Lien R C, Simmons H, et al. 2010. Speed and evolution of nonlinear internal waves transiting the South China Sea. Journal of Physical Oceanography, 40(6): 1338–1355, doi: 10.1175/2010JPO4388.1

Alford M H, Peacock T, Mackinnon J A, et al. 2015. The formation and fate of internal waves in the South China Sea. Nature, 528(7580): 65–69

Bourgault D, Galbraith P S, Chavanne C. 2016. Generation of internal solitary waves by frontally forced intrusions in geophysical flows. Nature Communications, 7: 13606, doi: 10.1038/ncomms13606

Cai Shuqun, He Jianling, Xie Jieshuo. 2011. Recent decadal progress of the study on internal solitons in the South China Sea. Advances in Earth Science (in Chinese), 26(7): 703–710

Cai Shuqun, Xie Jieshuo, Xu Jiexin, et al. 2014. Monthly variation of some parameters about internal solitary waves in the South China Sea. Deep Sea Research: Part I. Oceanographic Research Papers, 84: 73–85, doi: 10.1016/j.dsr.2013.10.008

Chen Chenyuan. 2012. RETRACTED: a critical review of internal wave dynamics. Part 2-Laboratory experiments and theoretical physics. Journal of Vibration and Control, 18(7): 983–1008, doi: 10.1177/1077546310397561

Cho C, Nam S H, Song H. 2016. Seasonal variation of speed and width from kinematic parameters of mode-1 nonlinear internal waves in the northeastern East China Sea. Journal of Geophysical Research: Oceans, 121(8): 5942–5958, doi: 10.1002/2016JC012035

Cox C, Munk W. 1954. Measurement of the roughness of the sea surface from photographs of the sun's glitter. Journal of the Optical Society of America, 44(11): 838–850, doi: 10.1364/JOSA.44.000838

Dossmann Y, Bourget B, Brouzet C, et al. 2016. Mixing by internal waves quantified using combined PIV/PLIF technique. Experiments in Fluids, 57(8): 132, doi: 10.1007/s00348-016-2212-y

Hsieh C M, Cheng M H, Hwang R R. 2016. Numerical study on evolution of an internal solitary wave across an idealized shelf with different front slopes. Applied Ocean Research, 59: 236–253, doi: 10.1016/j.apor.2016.06.006

Huang Xiaodong, Zhao Wei, Tian Jiwei, et al. 2014. Mooring observations of internal solitary waves in the deep basin west of Luzon Strait. Acta Oceanologica Sinica, 33(3): 82–89, doi: 10.1007/s13131-014-0416-7

Jackson C R, Alpers W. 2010. The role of the critical angle in brightness reversals on sunglint images of the sea surface. Journal of Geophysical Research: Oceans, 115(C9): C09019

Kodaira T, Waseda T, Miyata M, et al. 2016. Internal solitary waves in a two-fluid system with a free surface. Journal of Fluid Mechanics, 804: 201–223, doi: 10.1017/jfm.2016.510

Melsheimer C, Keong K L. 2001. Sun glitter in spot images and the visibility of oceanic phenomena. In: Proceedings of the 22nd Asian Conference on Remote Sensing. Singapore: CRISP

Song Shiyan, Wang Jing, Wang Jianbu, et al. 2010. Numerical simulation of internal waves propagation in deep sea by nonlinear Schrödinger equation. Acta Physica Sinica (in Chinese), 39(9): 818–823

Wang Jing, Guo Kai, Meng Junmin. 2012. Study of the propagation model for large-amplitude internal waves in deep sea. Chinese Journal of Lasers, 39(S2): 214004

Wang Juan, Huang Weigen, Yang Jingsong, et al. 2013. Study of the propagation direction of the internal waves in the South China Sea using satellite images. Acta Oceanologica Sinica, 32(5): 42–50, doi: 10.1007/s13131-013-0312-6

Yang Jingsong, Wang Juan, Ren Lin. 2017. The first quantitative remote sensing of ocean internal waves by Chinese GF-3 SAR satellite. Acta Oceanologica Sinica, 36(1): 118, doi: 10.1007/s13131-017-0999-x